PERGAMON

International Journal of Solids and Structures 39 (2002) 2533–2545

INTERNATIONAL JOURNAL OF SOLIDS and STRUCTURES

www.elsevier.com/locate/ijsolstr

Modeling the effects of hole distribution in perforated aluminum sheets II: minimum strength failure paths

S. Jia [1], G.L. Povirk [*,2]

Department of Mechanical Engineering, Yale University, New Haven, CT 06520 USA

Received 19 May 2001; received in revised form 20 January 2002

Abstract

A method to predict the failure path and mechanical response of metal sheets with randomly distributed holes under uniaxial tension has been developed. The method considers all possible failure paths and estimates the load required to break the perforated sheet along these paths. The predicted ultimate strength of the sheet is obtained by finding the failure path with the lowest possible load. The results from the model are compared to tensile experiments on a set of perforated aluminum sheets with different hole patterns. We found that the model, though relatively simple, could capture the effects that hole distribution had on the ultimate strength of the sheet. The ideas presented here could be extended to model the effect of reinforcement distribution in particle-reinforced composite materials. © 2002 Elsevier Science Ltd. All rights reserved.

Keywords: Fracture path; Composite; Reinforcement distribution; Ultimate strength; Tensile behavior

1. Introduction

In a previous effort Jia et al. (2002), we developed a method to determine periodic microstructures that were, in some sense, representative of the complex hole patterns that existed in the aluminum sheets. Finite element simulations of these "representative unit cells" were then used to estimate the mechanical properties of the sheets. While the representative unit cell method accurately predicted the behavior of the aluminum sheets, it has important limitations in terms of its application to a broader class of materials. Unfortunately, for a unit cell to actually be representative of many real composite microstructures, it would often have to be of such complexity that the corresponding finite element simulations would be computationally intractable, even for two-dimensional simulations.

In the present work, we sought to develop simpler methods that could predict the ultimate strength and ductility of perforated aluminum sheets. The basis of the current approach is to consider all possible failure

* Corresponding author. Address: 21 Chestnut Lane, 12309 Niskayuna, NY, USA. Tel.: +1-518-395-6709.
E-mail address: glpovirk@earthlink.net (G.L. Povirk).
[1] Present address: Structural Research and Analysis Corp., Los Angeles, CA 90025, USA.
[2] Present address: Knolls Atomic Power Laboratory, Schenectady, NY 12309, USA.

PII: S0020-7683(02)00116-6

paths and to estimate the ultimate strength associated with each path (the failure paths are assumed to proceed from hole to hole in the aluminum sheet). The predicted failure path is then simply the path with the lowest ultimate strength. This method requires estimates of the local mechanical behavior of the sheet as a function of the local length and orientation of a failure path segment. We obtained closed-form estimates of ultimate strength assuming perfect plasticity. In addition, local failure behavior was also modeled by performing finite element simulations of plastic flow between two adjacent holes. As in our previous study, model predictions of mechanical behavior will be compared to uniaxial tensile experiments performed on perforated aluminum sheets.

2. Method

Before we describe the model in detail, it will be useful to briefly review the experiments performed in our original study. Six different hole patterns were generated, each containing 115 holes with a net volume fraction of 10%. The patterns were printed onto sheets of paper, which in turn served as a template for the aluminum tensile samples. The aluminum sheets were perforated with a drill in the prescribed pattern, annealed, and finally subjected to standard uniaxial tensile tests. For every hole pattern, three tensile samples were fabricated.

To predict the failure path and the ultimate strength of the perforated metal sheet, we considered all feasible failure paths through the specimen, with the restriction that no "switchbacks" along the failure path were allowed (i.e., a path starting from the left hand side of the specimen must always proceed to the right hand side of the specimen). We further assumed that the failure path must lie upon line segments that connect the centers of holes and that the first and last line segments of the path are horizontal lines that connect the center of a hole to the edge of the sample. Even with these assumptions, there are numerous possible failure paths that need to be considered.

Each possible failure path was divided into n multiple strips as shown in Fig. 1. Each strip within the specimen contained a line segment connecting two half holes on each side of the strip. Strips that lay along the edge of the specimen had only one half hole with the other side being the sample edge. We now assume that each strip can be isolated and that plastic deformation can only occur along the line segments connecting the holes. Given that the plastic deformation was assumed to be confined to an area immediately surrounding the connecting line segment, we expect that the mechanical response of each strip will be affected by both the orientation θ and length l of the line segment. In addition, the tensile stress on the ith strip is assumed to depend on the normalized jump in displacement from the bottom to the top of the hole so that we can write

$$\varepsilon_{\text{path}} = \Delta u/2r$$

$$\sigma_i = \sigma(\varepsilon_{\text{path}}; l_i, \theta_i) \tag{1}$$

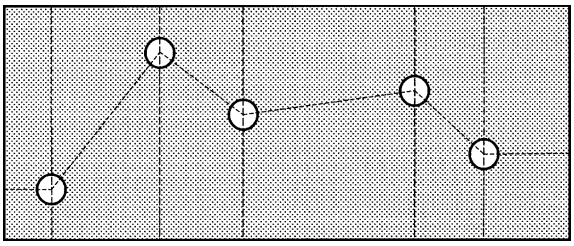

Fig. 1. Illustration of a failure path divided into multiple strips.

Here, Δu represents the difference in displacement across the hole, r is the hole radius and σ_i represents the axial "engineering" stress (force per unit original cross-sectional area) in the strip. The variable $\varepsilon_{\text{path}}$ is the strain associated with the failure path, which is identical to the axial strain across the hole. Compatibility between adjacent strips requires that at any point in the deformation the displacement jump Δu is the same for all of the strips. The mechanical response of the entire path is then simply the sum of the forces acting on all the strips divided by the total width of the specimen.

The macroscopic stress–strain behavior $\Sigma(\varepsilon_{\text{path}})$ is calculated for each possible failure path. Among all of the paths considered, the one with the lowest ultimate tensile strength is the predicted failure path. We used two approaches in developing expressions for the mechanical response of each strip: the first approach is a purely analytic derivation assuming perfect plasticity while the other involves finite element simulations of strips with various combinations of line segment length and orientation.

2.1. Analytic approach

We assume that the material can be characterized as a rigid, isotropic, and perfect plastic material that yields according to the Tresca (maximum shear stress) criterion. Given this assumption, the response of a given strip will be independent of both the strain $\varepsilon_{\text{path}}$ and line segment length l_i so that $\sigma(\varepsilon_{\text{path}}; l_i, \theta_i)$ can be written more simply as $\sigma(\theta_i)$. The assumption of perfect plasticity limits us in that the stress–strain behavior of the sheet cannot be predicted. However, the analysis will provide estimates of ultimate strength and predicted failure paths that can be compared with experiments.

We begin by ignoring the effects of the holes and considering a straight strip of material with width w, thickness b, height h, line segment length l, and orientation angle θ (see Fig. 2). The line segment length represents the distance between the edges of adjacent holes and not the distance between hole centers. In effect, we are assuming that the material directly above and below each hole does not contribute to the load carrying capacity of the structure. Because all of the plastic deformation is presumed to localize along the line segment, we will assume that a plane of maximum shear stress passes through the line segment with normal $\hat{n}$ and slip direction $\hat{s}$. The unit vector along the line segment is $\hat{l} = (\cos\theta, \sin\theta, 0)$ and the tensile

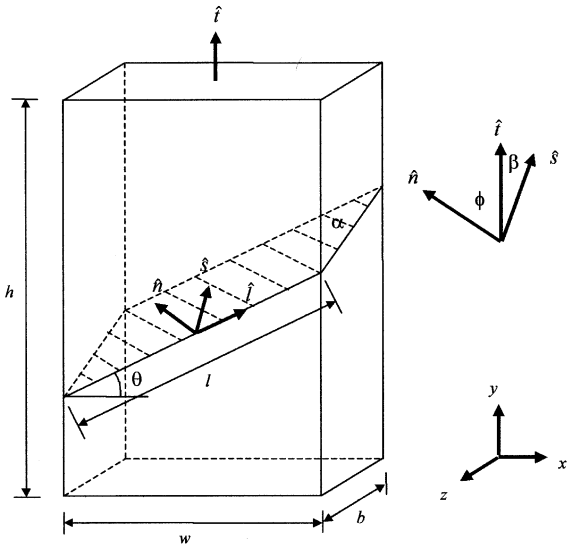

Fig. 2. Schematic of a shear band within a strip of metal.

axis is given by $\hat{t} = (0, 1, 0)$. We will denote the angle between $\hat{n}$ and $\hat{t}$ as ϕ and the angle between $\hat{s}$ and $\hat{t}$ as β. Without loss of generality, we also assume that $0 \leqslant \phi \leqslant \pi/2$ and $0 \leqslant \beta \leqslant \pi/2$ (reversing the direction of either the slip plane normal or the slip direction merely changes the sign of the shear stress).

Our goal is to determine the relationship between the tensile stress σ_i and the angle of the localized plastic deformation θ_i. The relationship between the tensile stress σ_i required for yielding and the yield strength in shear, τ_y, is given by

$$\sigma_i = \frac{\tau_y}{m_{\max}} \tag{2}$$

where

$$m_{\max} = \max\{|(\hat{t} \cdot \hat{n})(\hat{t} \cdot \hat{s})|\} = \max\{|\cos\phi \cos\beta|\} \tag{3}$$

The maximum value of the Schmid factor, $m_{\max}$, will depend on the specific boundary conditions that we apply to the sides of the material strip. Compatibility between adjacent strips suggests that there should be no relative displacement of material across the slip plane in the x-direction. However, for the actual problem under consideration, the slip planes will terminate at the free surfaces of holes, which in turn suggests that relative motions in the x-direction would be kinematically permissible. We will consider the effect of each of these assumptions on the mechanical response of the strip. These conditions on the deformation will be denoted as "fixed" and "free" boundary conditions, respectively.

2.1.1. Free boundary conditions

For a given angle θ and applied stress σ_i, we wish to find the orientation of the slip plane normal $\hat{n}$ and the slip direction $\hat{s}$ that will result in the maximize shear stress. In other words, for a prescribed angle θ we want to determine the values of ϕ and β that will maximize the quantity $m = |\cos\phi \cos\beta|$. Note that $\hat{n} \cdot \hat{l} = 0$ because the slip plane passes through the line segment l, and that, by definition, $\hat{n} \cdot \hat{t} = \cos\phi$. Finally, given that $\hat{n}$ is a unit vector, we have

$$\begin{cases} n_2 = \cos\phi \\ n_1 \cos\theta + n_2 \sin\theta = 0 \\ n_1^2 + n_2^2 + n_3^2 = 1 \end{cases} \Rightarrow \begin{cases} n_1 = -\cos\phi \tan\theta \\ n_2 = \cos\phi \\ n_3 = \pm\sqrt{1 - (\cos^2\phi / \cos^2\theta)} \end{cases} \tag{4}$$

In order for n_3 to be a real number, we have the restriction that $\phi \geqslant \theta$. In addition, the fact that $\hat{n}$ and $\hat{s}$ are perpendicular to one another imposes an additional constraint on the value of β

$$\frac{\pi}{2} - \phi \leqslant \beta \leqslant \frac{\pi}{2} \tag{5}$$

The maximum possible value for the $\cos\beta$ therefore occurs when $\beta = \pi/2 - \phi$. The Schmid factor now takes the form

$$m = |\cos\phi \sin\phi| = \tfrac{1}{2}|\sin 2\phi| \tag{6}$$

In general, the above expression is maximized when $\phi = \pi/4$. Recall, however, from Eq. (4) that the value of ϕ is restricted by the relationship $\phi \geqslant \theta$. Therefore, the maximum value of m can be written in the following form

$$m_{\max} = \begin{cases} \frac{1}{2}, & \text{for } 0 \leqslant \theta \leqslant \pi/4 \\ \frac{1}{2}\sin 2\theta, & \text{for } \pi/4 \leqslant \theta \leqslant \pi/2 \end{cases} \tag{7}$$

The expression for the tensile strength of a given strip therefore becomes

$$\sigma(\theta_i) = \begin{cases} 2\tau_y, & \text{for } 0 \leqslant \theta_i \leqslant \pi/4 \\ 2\tau_y / \sin 2\theta_i, & \text{for } \pi/4 \leqslant \theta_i \leqslant \pi/2 \end{cases} \tag{8}$$

The above expression becomes unbounded as $\theta_i \to \pi/2$. It will prove useful to define a slightly different quantity, $S(\theta_i) = \sigma(\theta_i)\cos(\theta_i)$, which represents the force per unit length of connecting line segment per unit thickness. For the free boundary conditions, this quantity takes the form

$$S(\theta_i) = \begin{cases} 2\tau_y \cos\theta_i, & \text{for } 0 \leqslant \theta_i \leqslant \pi/4 \\ \tau_y / \sin\theta_i, & \text{for } \pi/4 \leqslant \theta_i \leqslant \pi/2 \end{cases} \tag{9}$$

2.1.2. Fixed boundary conditions

The key assumption here is that slip in the x-direction is forbidden so that compatibility with adjacent strips is maintained. With this assumption, the slip direction can be written simply as $\hat{s} = (0, \cos\beta, -\sin\beta)$. Noting that the slip plane normal $\hat{n}$ is perpendicular to both the slip direction $\hat{s}$ and the direction of the line segment $\hat{l}$, we can obtain components of the slip plane normal in terms of the angles ϕ, β, and θ

$$\begin{cases} \hat{n}\cdot\hat{t} = \cos\phi \\ \hat{n}\cdot\hat{l} = 0 \\ \hat{n}\cdot\hat{s} = 0 \end{cases} \Rightarrow \begin{cases} n_2 = \cos\phi \\ n_1\cos\theta + n_2\sin\theta = 0 \\ n_2\cos\beta - n_3\sin\beta = 0 \end{cases} \Rightarrow \begin{cases} n_1 = -\cos\phi\tan\theta \\ n_2 = \cos\phi \\ n_3 = \cos\phi/\tan\beta \end{cases} \tag{10}$$

Further noting that $\hat{n}$ is a unit vector, we can express the angle ϕ in terms of β and θ

$$\cos^2\phi = \frac{1}{1 + \tan^2\theta + \cot^2\beta} \tag{11}$$

Substituting the above equation into the expression for the Schmid factor (Eq. (3)) gives

$$m^2 = \cos^2\phi\cos^2\beta = \cos^2\beta/(1 + \tan^2\theta + \cot^2\beta) \tag{12}$$

Inverting the above equation allows for a relatively simple expression of the Schmid factor in terms of $\tan^2\theta$ and $\cos^2\beta$

$$\frac{1}{m^2} = \frac{\tan^2\theta}{\cos^2\beta} + \frac{1}{\cos^2\beta(1-\cos^2\beta)} \tag{13}$$

By minimizing the expression for $1/m^2$ with respect to $\cos^2\beta$, it can be shown that the Schmid factor is maximized when

$$\cos^2\beta = \frac{1}{1+\cos\theta} \tag{14}$$

which results in the following expression for $m_{\max}$

$$m_{\max} = \frac{\cos\theta}{1+\cos\theta} \tag{15}$$

Substituting into Eq. (2), the axial stress within a given strip takes the following form

$$\sigma(\theta_i) = \frac{\tau_y(1+\cos\theta_i)}{\cos\theta_i} \tag{16}$$

Again, note that the expression for the axial stress in the strip becomes unbounded as $\theta_i \to \pi/2$. In terms of the quantity $S(\theta_i) = \sigma(\theta_i)\cos(\theta_i)$ defined earlier, the response of the strip is given by

$$S(\theta_i) = \tau_y(1+\cos\theta_i) \tag{17}$$

For either set of boundary conditions, the ultimate strength of a fracture path, Σ, is given by the following expression

$$\Sigma = \frac{\sum_{i=1}^{n} \sigma(\theta_i) l_i \cos\theta_i}{w} = \frac{\sum_{i=1}^{n} S(\theta_i) l_i}{w} \tag{18}$$

where w is the total width of the tensile sample.

2.2. Finite element approach

In contrast to the analytic approach where we assumed perfect plasticity, the power of finite elements allows us to incorporate material hardening into a complete boundary value problem for a given material strip. In this case, then, we can assume that the flow strength of each strip will take the more general form of $\sigma_i = \sigma(\varepsilon_{\text{path}}; l_i, \theta_i)$. By considering strips with various values of l_i and θ_i we can develop an approximate description of the mechanical response of a strip with a line segment of arbitrary angle and length. We did, however, find it more useful to characterize the response of the strip in terms of the normalized force

$$S(\varepsilon_{\text{path}}; l_i, \theta_i) = \sigma(\varepsilon_{\text{path}}; l_i, \theta_i)\cos(\theta_i)(l_i + 2r)/l_i \tag{19}$$

Using this quantity allows us to avoid the expected singular behavior as $\theta_i \to \pi/2$ as it was the for the analytic approaches.

We begin by considering a strip of material with two half holes on each side as shown in Fig. 3. The strip is loaded in tension by applying a uniform displacement rate $\dot{V}$ to the top surface of the strip. To enforce compatibility with surrounding strips, the sides of the region are required to remain straight. The boundary conditions for the displacements $u_x(x,y)$ and $u_y(x,y)$ can be summarized as follows

$$\begin{aligned} &u_y(x,0) = 0, \quad u_y(x,h) = V \\ &u_x(0,y) = 0, \quad u_x(w,y) = U \end{aligned} \tag{20}$$

where U and V are only functions of time. In addition, because we are simulating a state of uniaxial tension, we will require that the net traction acting on the sides of the strip vanishes, i.e.,

$$\int_{y=0}^{y=h} \hat{T}(0,y)\,\mathrm{d}y = \int_{y=0}^{y=h} \hat{T}(w,y)\,\mathrm{d}y = 0 \tag{21}$$

where $\hat{T}(x,y)$ are the surface tractions. Also note from Fig. 3 that the material immediately surrounding the connecting line segment l is treated as elastic–plastic while the material outside of this region is assumed to have only elastic behavior. This assumption is necessary to force failure along the line segment l for all values of the orientation angle θ. At lower angles, where this assumption is not necessary, we also performed calculations with a completely elastic–plastic material strip. We found that the assumption of pure elastic behavior outside of the region of localized plastic deformation did not significantly affect the predicted behavior.

The plastic behavior of the aluminum was assumed to be rate-independent J_2 flow theory with isotropic hardening. The hardening behavior was obtained by tensile experiments on annealed, non-perforated, 1100 aluminum sheets and (see Fig. 4). For simplicity, we did not model any strain softening in the aluminum. Instead, we assumed perfectly plastic behavior after the material reached its peak stress. Finite strain kinematics were employed in conjunction with the material constitutive law because of the large strains that develop during the analysis. Finally, quasi-static deformations were presumed so that equilibrium takes the standard form of $\nabla \cdot \sigma = 0$, where σ is the stress tensor.

Solutions to the boundary value problems described above were obtained using the commercial finite element code ABAQUS (1997). Calculations were performed using two-dimensional, four node, plane stress

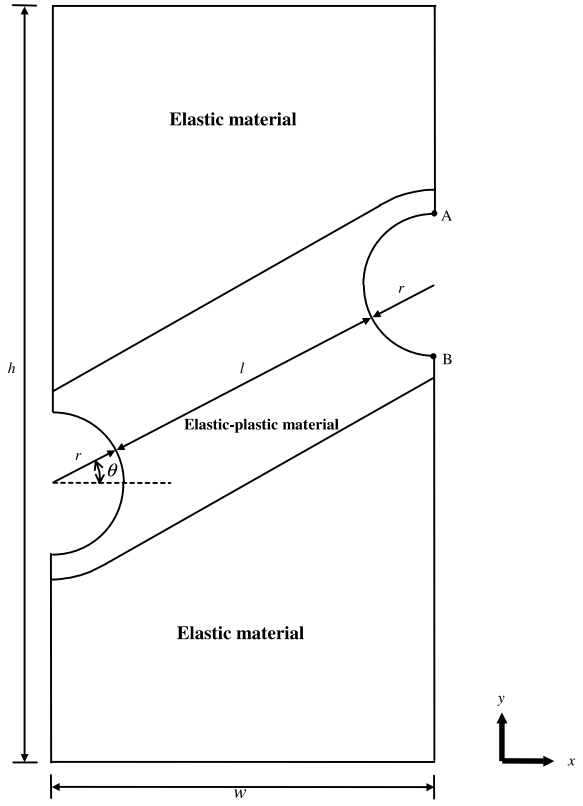

Fig. 3. Finite element model of a strip containing a line segment with two half holes on each end.

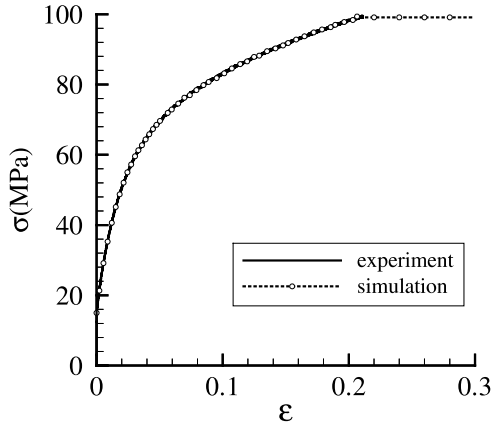

Fig. 4. Behavior of commercially pure aluminum from tensile experiment.

elements. In addition, numerous calculations were performed with a full, three-dimensional representation of the material strips using eight node brick elements. We found that the results from the three-dimensional models did not significantly differ from those of the plane stress model. All of the reported results, therefore, are from the plane stress case.

The goal of the simulations is to predict the mechanical response of a strip with arbitrary length and orientation of the connecting line segment. The normalized force $S(\varepsilon_{\text{path}}; l_i, \theta_i)$ was calculated at any instant of time simply by summing all of the nodal axial forces from the top surface of the strip and divided by the original line segment length l and original thickness. Likewise, the strain across the hole was given by $\varepsilon_{\text{path}} = (u_y^A - u_y^B)/2r$. An advantage to characterizing the deformation in terms of the hole expansion instead of the extension of the whole strip is that the latter depends on the height of the strip h while the former is independent of h. In other words, otherwise identical strips with different height h give different predicted stress–strain curves if the strain is based on the extension of the entire strip. In contrast, the behavior becomes independent of h if the strain is measured across the hole.

The response of the strips given by the curves $S(\varepsilon_{\text{path}}; l_i, \theta_i)$ was fit with the following function

$$S_i = S(\varepsilon_{\text{path}}; l_i, \theta_i) = \begin{cases} S_y + (S_{\max} - S_y)\left(1 - \left(\frac{\varepsilon_{\text{path}} - \varepsilon_1}{\varepsilon_1}\right)^2\right)^n, & \text{for } 0 \leqslant \varepsilon_{\text{path}} \leqslant \varepsilon_1 \\ \frac{1}{2} S_{\max}\left(1 + \cos\left(\pi \frac{\varepsilon_{\text{path}} - \varepsilon_1}{\varepsilon_2 - \varepsilon_1}\right)\right), & \text{for } \varepsilon_1 \leqslant \varepsilon_{\text{path}} \leqslant \varepsilon_2 \end{cases} \tag{22}$$

where the parameters S_y, $S_{\max}$, ε_1, ε_2, m were, in general, all assumed to be functions of l_i and θ_i. As with the analytic approach, the macroscopic stress–strain behavior for the entire path is simply the sum of the forces acting on each strip divided by the total width of the sample

$$\Sigma(\varepsilon_{\text{path}}) = \frac{\sum_{i=1}^{n} \sigma_i(\varepsilon_{\text{path}}; l_i, \theta_i)(l_i + 2r)\cos\theta_i}{w} = \frac{\sum_{i=1}^{n} S_i(\varepsilon_{\text{path}}; l_i, \theta_i) l_i}{w} \tag{23}$$

3. Results

For the finite element approach, recall that the response of a given strip $S(\varepsilon_{\text{path}}; l_i, \theta_i)$ was characterized by the parameters S_y, $S_{\max}$, ε_1, ε_2, and n which were, in general, all assumed to be functions of l_i and θ_i (see Eq. (22)). By performing finite element analyses on a series of different strips, we could ascertain the dependence of these parameters on the length l_i and angle θ_i. For example, the behavior of the ultimate strength, $S_{\max}(l, \theta)$, is shown in Fig. 5 while the measure of ductility, $\varepsilon_1(l, \theta)$, is given in Fig. 6. Good fits to the finite element results were obtained by assuming that the parameters S_y and n were independent of length and angle, with values of $S_y = 0$ and $n = 0.35$. Lastly, using $\varepsilon_2(l, \theta) = 2\varepsilon_1(l, \theta)$ gave a reasonable fit to the eventual load drop predicted by the finite element calculations.

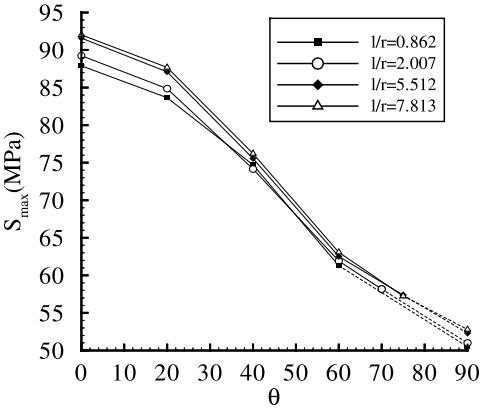

Fig. 5. Strip strength per unit length as a function of segment angle and segment length from finite element simulations, where r represents the radius of the holes. Dashed lines represent extrapolations to high shear band angles.

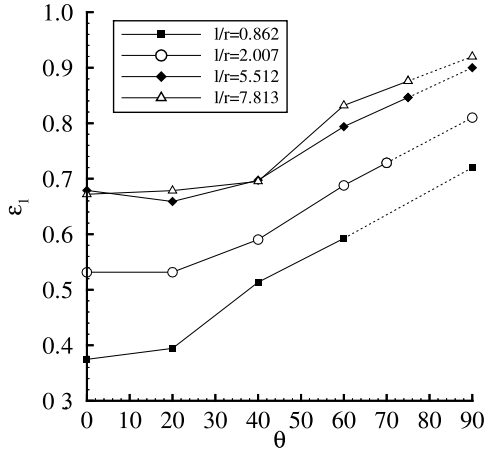

Fig. 6. Strip ductility as a function of segment angle and segment length from finite element simulations, where r represents the radius of the holes. Dashed lines represent extrapolations to high shear band angles.

The behavior of $S_{\max}(l,\theta)$ is interesting in that it can be compared to the analytic results developed in Section 2. Qualitatively, the curves generated for $S_{\max}(l,\theta)$ from the finite element results are quite similar to the yield strength predictions given in Eq. (9) for the "free" boundary conditions and Eq. (17) for the "fixed" boundary conditions. In fact, if the curves for $S_{\max}(l,\theta)$ are normalized, they fall between those predicted by the "fixed" and "free" boundary conditions. The fact that $S_{\max}(l,\theta)$ is almost independent of the length l is likely a consequence of our assumption of perfect plasticity after the maximum flow strength of the aluminum is reached. In contrast, the ductility $\varepsilon_1(l,\theta)$ (see Fig. 6) shows a strong dependence on length when l/r is small, but much less so as l/r is increased. This is expected because the influence of the holes should diminish as the length of the shear band increases.

Fig. 7 compares the fracture paths observed experimentally to those predicted by the analytic approach with "fixed" boundary conditions, "free" boundary conditions, and the finite element approach, respectively. In each figure, the most common fracture paths observed experimentally are indicated by the solid lines while the less common fracture paths are shown with dotted lines (recall that for each hole pattern, three samples were fabricated and tested). The results from the theories are given in a similar manner. For a given hole pattern and approach, we plotted the failure paths associated with the 10 lowest values of the predicted ultimate strength. The expected failure path is the one with the lowest ultimate strength and is indicated with the solid line. It is worth noting that for any hole pattern, the difference between the 10 lowest values of the predicted ultimate strength was at most 3.5%.

A cursory examination of the figures suggests that all of the methods seem to have roughly the same level of agreement (and disagreement) between the predicted paths and those observed experimentally. A closer examination of the results, however, indicate that the analytic approach with the "fixed" conditions and the finite element approach most often produce the best agreement with the experiments. Conversely, the analytic approach with the "free" boundary conditions appears to have the poorest correlation between theory and experiment. To quantify these discrepancies between theory and experiment, we calculated the differences in theoretical ultimate strengths between the weakest predicted failure path and the path most often seen experimentally (see Table 1). The results show that the strength of the weakest path obtained with the "fixed" analytic approach was typically very close to the theoretical strength of the experimentally observed path. In contrast, the analytic "free" approach usually had the largest difference between the calculated strength of the weakest path and the predicted strength of the experimental path.

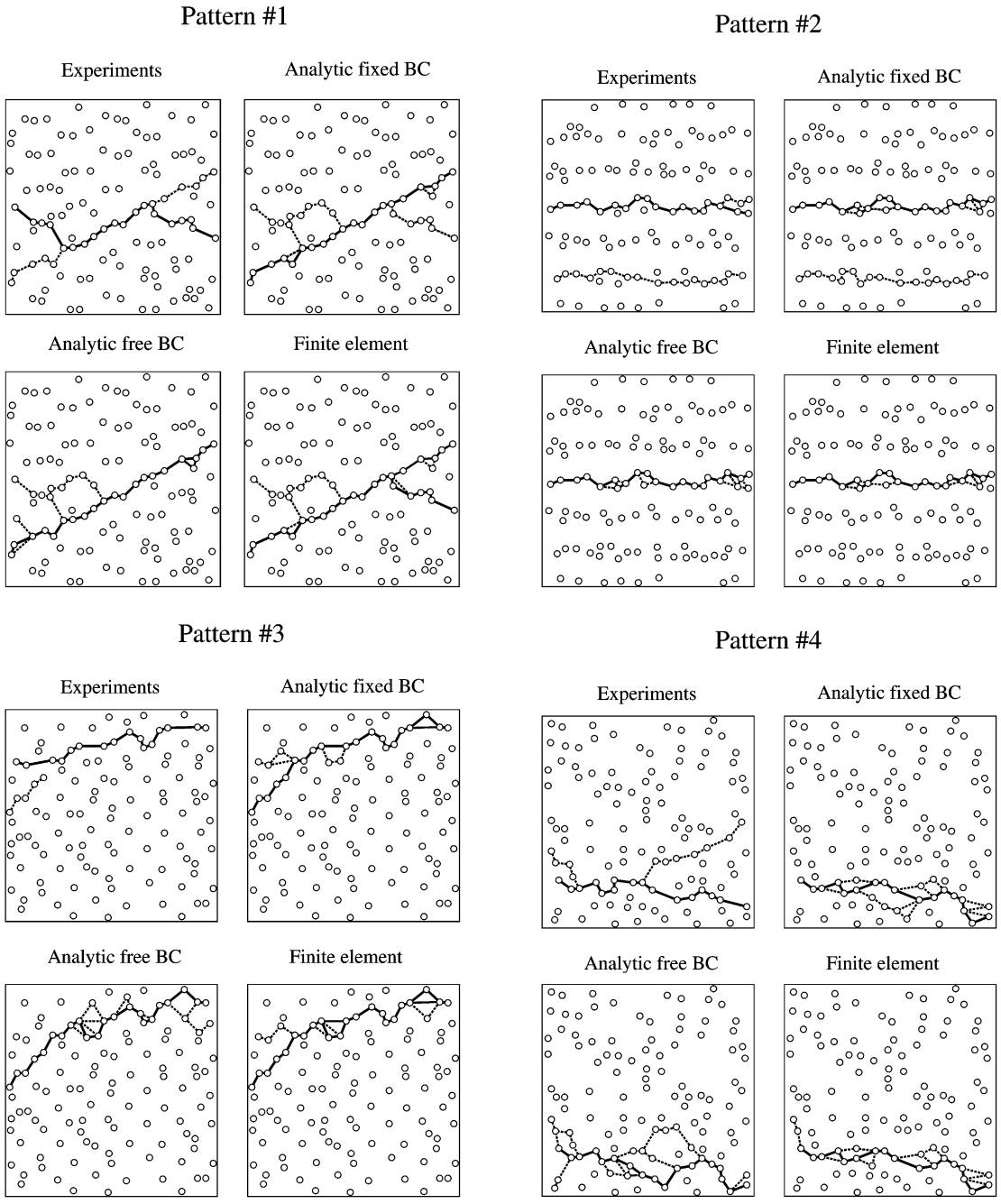

Fig. 7. Comparison between experimentally observed and predicted failure paths.

Fig. 8 shows the correlation between predicted and experimentally measured ultimate tensile strengths. Since the strengths predicted by analytic approaches are relative to an assumed shear strength, they were normalized by a factor to be comparable to predictions by the finite element approach. The theoretical

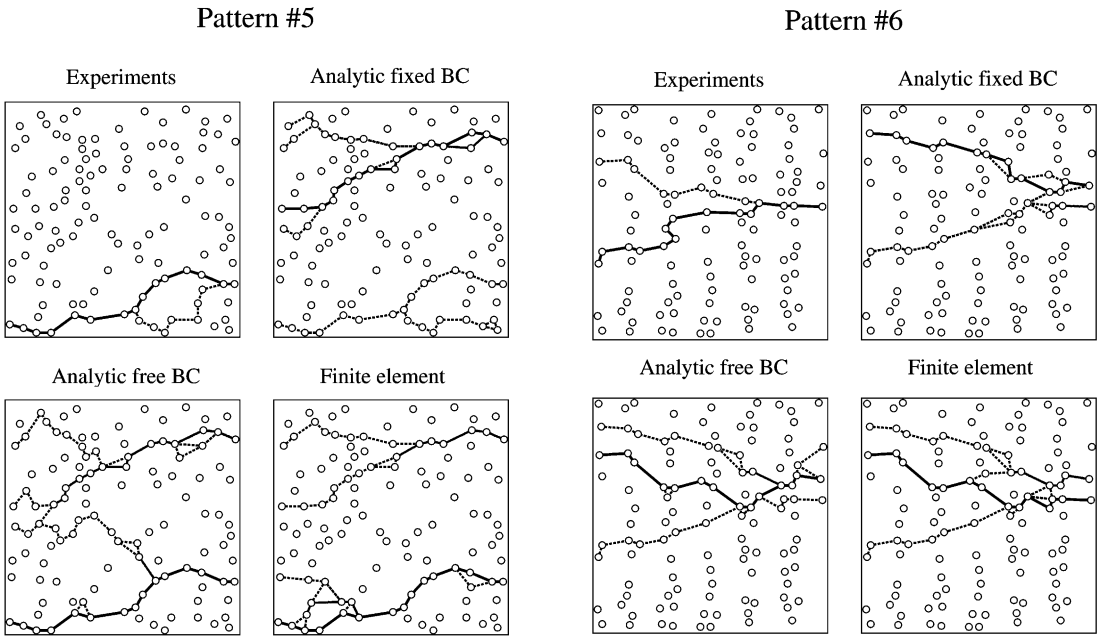

Fig. 7 (*continued*)

Table 1
Difference in predicted ultimate strength between the weakest theoretical failure path and experimentally observed failure path

Pattern	Analytic "fixed BCs"	Finite element approach	Analytic "free BCs"
#1	0%	0.28%	0%
#2	0.68%	0.86%	1.02%
#3	1.68%	7.50%	12.37%
#4	1.50%	2.28%	4.75%
#5	0.25%	0%	0%
#6	2.51%	3.20%	4.57%

strengths represent the absolute lowest strength predicted by any of the failure paths for a given hole pattern. The slopes of linear fit lines are 1.18 for the analytic approach with "fixed" boundary conditions, 1.19 for the analytic with "free" boundary conditions, and 1.22 for the finite element approach. The fit associated with the finite element calculation also comes close to passing through the origin, which suggests that procedures were successful in predicting the magnitudes of the ultimate strengths. Overall, it appears that the analytic approach with the "fixed" boundary conditions is most consistent in predicting the trends in ultimate strength.

4. Discussion

We find the results from the current model to be quite encouraging. In comparison with our previous effort Jia et al. (2002), the fracture path-based method described here is much simpler and computationally less intensive. As Fig. 8 shows, its predictions of ultimate strength (analytic with "fixed" boundary conditions) are comparable to the representative unit cell method. Given the difficulty in successfully predicting

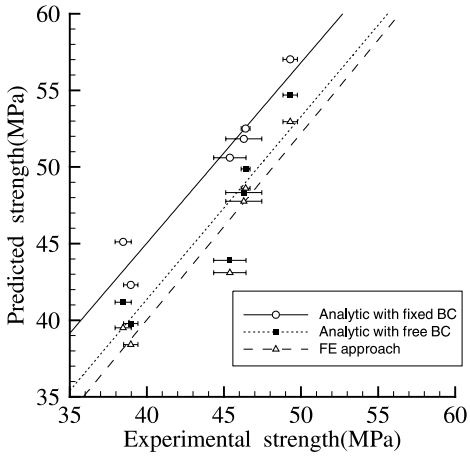

Fig. 8. Predicted ultimate strengths of the perforated aluminum sheets compared to experimental results. Horizontal bars represent the range of strength variations for the three samples of each hole pattern exhibited in the experiments.

fracture paths, we are optimistic that further refinements in the model could result in a simple yet useful tool for evaluating the role of reinforcement distribution on mechanical properties.

One surprising result is that the analytic method (with "fixed" boundary conditions) had better agreement in terms of both the fracture paths as well as the trends in ultimate strength when compared to the finite element-based approach. This is remarkable given that the power of finite elements allowed for both more realistic modeling of material behavior and a more complex geometry that accounted for the presence of the holes. The reason for this surprising result is unclear, although two possibilities come to mind. First, in the finite element-based procedures we assumed that the region outside of the shear band had perfectly elastic behavior. While we determined that this assumption did not significantly alter the results at small shear band angles, we do not know if the effect is significant at larger angles. A second possibility is our assumption regarding the behavior of the aluminum matrix. For simplicity we assumed perfectly plastic behavior in the aluminum once its ultimate strength was reached. A more realistic model would have incorporated strain softening into the analysis, as we did in our previous study.

In terms of future efforts, one possibility for refining the model is to borrow the idea of a "critical crack length" from work of Ibnabdeljalil and Curtin (1997) on the failure of long-fiber reinforced composites. In the work described here, we have implicitly assumed that the strength of the *entire* fracture path was the controlling aspect of predicted strength of the aluminum sheets. For brittle materials, it is probably more appropriate to assume that failure will first initiate on the weakest path that is of some pre-defined critical length. Once a crack is formed, the final failure path will result from the propagation of the crack. For ductile materials, a similar concept might prove to be useful, although we would expect the critical length for ductile materials to be larger than for a corresponding brittle material.

We believe that the methods described herein have the potential to develop into a practical tool for evaluating the effects of reinforcement distribution on the mechanical properties of composite materials. Further studies on actual composites are required, however, if these ideas are to be accepted into practice.

Acknowledgements

The authors are pleased to acknowledgement financial support provided by the Air Force Office of Scientific Research, contract number F49620-96-1-0198. This paper is dedicated to the memory of Prof. E.T. Onat, who suggested the approach used in this paper.

References

Jia, S., Raiser, G.F., Povirk, G.L., 2002. Modeling the effects of hole distribution in perforated aluminum sheets I: representative unit cells. Int. J. Solids Struct. 39 (9), 2517–2532.

ABAQUS™, version 5.7, Hibbitt, Karlsson & Sorensen, Inc., 1997, www.hks.com.

Ibnabdeljalil, M., Curtin, W.A., 1997. Strength and reliability of fiber-reinforced composites: localized load-sharing and associated size effects. Int. J. Solids Struct. 34 (21), 2649–2668.